Solar Energy Materials & Solar Cells 157 (2016) 318–325

Contents lists available at ScienceDirect

Solar Energy Materials & Solar Cells

journal homepage: www.elsevier.com/locate/solmat

Solution processed perovskite solar cells using highly conductive PEDOT:PSS interfacial layer

Getachew Adam [a], Martin Kaltenbrunner [b], Eric Daniel Głowacki [a], Dogukan Hazar Apaydin [a], Matthew Schuette White [a], Herwig Heilbrunner [a], Sekai Tombe [a,c], Philipp Stadler [a], Bruno Ernecker [d], Christian Wolfgang Klampfl [d], Niyazi Serdar Sariciftci [a], Markus Clark Scharber [a,*]

[a] Linz Institute for Organic Solar Cells (LIOS), Institute of Physical Chemistry, Johannes Kepler University Linz, Altenbergerstr. 69, 4040 Linz, Austria
[b] Department of Soft Matter Physics, Johannes Kepler University Linz, Altenbergerstr. 69, 4040 Linz, Austria
[c] Sensor Lab Department of Chemistry, University of Western Cape, Private Bag X17, Bellville, 7535 Cape Town, South Africa
[d] Institute for Analytical Chemistry, Johannes Kepler University Linz, Altenbergerstr. 69, 4040 Linz, Austria

ARTICLE INFO

Article history:
Received 7 December 2015
Received in revised form
25 April 2016
Accepted 4 May 2016

Keywords:
Solar cell
Hybrid organic inorganic
Perovskite
Solution processing

ABSTRACT

We have developed a simple and robust process to prepare efficient perovskite solar cells. Pinhole free thin films of $CH_3NH_3PbI_{3-x}Cl_x$ can be coated on high conductivity poly(3,4-ethylenedioxythiophene) poly(styrene-sulfonate) (PEDOT:PSS), (Clevios PH1000) when the PEDOT:PSS is deposited together with dimethyl sulfoxide (DMSO) and Zonyl as additives. This process enables the fabrication of perovskite solar cells using [6,6]-phenyl-C_{61}-butyric acid methyl ester (PCBM) as electron transport layer with $>12\%$ power conversion efficiency, low hysteresis and excellent operational stability. We have performed a detailed opto-electronic characterization of these solar cells and identified the main loss mechanism limiting the device performance.

1. Introduction

Efficient, easily processable and low-cost solar cell absorber materials represent the core-target of current photovoltaic research. Organic-inorganic hybrid perovskites based on methyl ammonium lead tri-halide compounds excellently fit the mentioned requirements; their light harvesting properties are tunable by varying the chemical composition, their processing is simple and power-conversion is efficient [1]. Interestingly, these perovskite semiconductors exhibit balanced electron and hole mobilities, long-range diffusion length and long recombination life time of charge carriers [2–4]. The precursors for organic-inorganic hybrid perovskites are readily available at relatively low costs, and can be processed from solution onto rigid or flexible substrates using printing compatible methods [5–11]. The rapid development in device design and fabrication techniques has led to a tremendous increase in the power conversion efficiencies (PCE) of perovskite solar cells in a short period of time from 3% to 4% in 2009 [12] to $>20\%$ in 2015 [5–7].Theoretical calculations project the power conversion efficiency to approach the Shockley–Queisser limit of 31.4% [13,14].

Despite the remarkable progress in record cell efficiency, three significant hurdles remain for perovskite photovoltaic technology:

1) Improving the long-term stability of the cells,
2) Defining standard characterization protocols to eliminate hysteresis artifacts, and
3) Forming pinhole-free films of the highly crystalline semiconductor over large areas.

While promising stability data were reported for mesoscopic devices built on TiO_2 and ZrO_2 [11], the high efficiency device stack reported using ITO/PEIE/Y-TiO_2/perovskite/spiro-OMeTAD/Au degrades even in inert atmosphere and in dark within a few hours [5].

Defining the efficiency of perovskite solar cells presents also a challenge compared to more conventional PV technologies. Typically, device efficiencies are extracted from current density–voltage (J–V) curves, which are recorded by sweeping an applied bias across the terminals of the cell and simultaneously measuring the current flowing in the external circuit while the solar cell is exposed to a well-defined or standard light source. Many devices reported in the literature show a strong hysteresis, *i.e.* their J–V

* Corresponding author.
E-mail addresses: getachew_adam.workneh@jku.at (G. Adam), markus_clark.scharber@jku.at (M.C. Scharber).

http://dx.doi.org/10.1016/j.solmat.2016.05.011
0927-0248/

curve depends on the sweep direction and also on the bias sweep rate [15–18]. This hysteresis leads to a significant deviation in the measured efficiency depending on the procedure. Precautions for addressing stability and hysteresis during device characterization have been suggested [19].

Reproducible production of pinhole-free films over large areas is an absolute requirement for both commercial fabrication and lab-scale research. Several successful device architectures have been reported with varying electron and hole selective contact materials. Perovskite semiconductors have been coupled with either a planar or mesoporous n-type metal oxide (TiO_2, Al_2O_3, ZrO_2, ZnO) and an organic hole-transport material (HTM) as selective contacts for charge extraction [10,11,20–22]. Planar device structures have also been demonstrated using non-oxide n-type materials like fullerene, as an electron selective contact and a p-type HTM. A typical device stack comprises PEDOT:PSS as p-type material, the organic-inorganic hybrid perovskite as absorber layer and a fullerene derivative as electron selective contact [23–26]. The oxide-free architecture can be solution processed at low temperatures on light weight flexible substrates [27,28]. In all cases, the preparation of pinhole and defect-free perovskite layers is required to optimize device performance. Various processes for making high quality films have been reported. These include vacuum deposition, by co-evaporation of PbI_2 with CH_3NH_3I [9], sequential solution depositions of the two components (spin coating followed by dip coating or two spin coating steps) [8,10,22], spin coating just from one precursor solution [5], and vapor assisted solution processing (*e.g.* the film growth via reaction of the as deposited film of PbI_2 with CH_3NH_3I vapor) [29]. Approaches using different solvent combinations (solvent engineering) have also shown promising results [26,30]. Solution processing, particularly deposition from a single precursor solution, is in-principle the simplest approach to make perovskite films. However, it has been found that the formation of the perovskite films depends heavily on the processing parameters including the wettability and the chemical compatibility of the underlying surface. Perovskite precursor solutions spin coating recipes, solvent treatment and annealing temperature and times are varied accordingly. Some examples of processing recipes include: a stoichiometric mixture of PbI_2 and CH_3NH_3I dissolved in DMF or DMSO [24], $PbCl_2+3CH_3NH_3I$ dissolved in DMF [20,22], excess CH_3NH_3I by using $PbI_2+3CH_3NH_3I$ [31], and adding a small amount of either CH_3NH_3Cl or CH_3NH_3Br in the host solution of PbI_2 and CH_3NH_3I [32,33].

Processing perovskite solar cells from a single precursor perovskite ink shows a clear possibility of role to role industrial scale production of perovskite solar cells especially when using solution processed polymeric materials instead of high temperature and vacuum processed inorganic oxides as interlayers [34]. Recently high performance solution processed perovskite solar cells without an additional hole transport layer have been reported [35]. Blade-coated perovskite solar cells reported by the Jen-group [36] support the idea that used material and processes are fully printing compatible.

In this work we prepared solar cells based on a planar heterojunction architecture (indium tin oxide (ITO)/ PEDOT:PSS / $CH_3NH_3PbI_{3-x}Cl_x$/[6,6]-phenyl-C_{61}-butyric acid methyl ester (PCBM)/ aluminum). We found that the used PEDOT:PSS formulation is critical for the quality of the perovskite layer deposited on top of it and best device performance is obtained when 5% v/v DMSO and 0.7% v/v Zonyl® FS-300 fluoro-surfactant are added to the commercially available Clevios PH1000 dispersion. The recipe is highly reproducible under standard ambient laboratory conditions and does not require special humidity control.

Prepared devices showed minimal hysteresis in their J-V curves, good stability when operated under inert atmosphere or after encapsulation and power conversion efficiencies in the range of 12–13%. A detailed optoelectronic analysis allowed us to determine the losses limiting the power conversion efficiency of the investigated devices [37].

2. Experimental details

Pre-patterned indium doped tin oxide (ITO) coated glass (15 Ω/cm^2), PbI_2 (99.9%, Sigma Aldrich), $PbCl_2$ (99.9%, Sigma Aldrich), methylammonium iodide (Dyesol), dimethylformamide (DMF, dry, Sigma Aldrich), poly(3,4-ethylenedioxythiophene) poly (styrenesulfonate) (PEDOT:PSS, Clevios pH 1000), Zonyl® FS-300 fluorosurfactant (40% in H_2O, Fluka), dimethyl sulfoxide (DMSO, Anal R, VWR chemicals), [6,6]-phenyl-C_{61}-butyric acid methyl ester (PCBM, SolenneBV), chlorobenzene (GPR, VWR chemicals), chloroform (Anal R, VWR chemicals), isopropanol (Anal R, Fisher chemicals) were used as received. Precursor mixed halide solutions were prepared with molar ratio ($0.5PbCl_2+0.5PbI_2+2.2CH_3NH_3I$) (640 mg/ml in DMF) stirred overnight at room temperature in ambient air and filtered with 0.45 μm PTFE filter. Perovskite thin films for UV–vis optical absorption and photoluminescence measurements were prepared by spin-coating at 4000 rpm on different substrates from 50% diluted solution of the precursor solution. The fabrication of planar heterojunction perovskite solar cells started with cleaning pre-patterned ITO coated glass substrates sequentially with acetone, Hellmanex®, deionized water and isopropanol in an ultrasonic bath. Different volumes of PEDOT:PSS (Clevios PH1000), DMSO and Zonyl FS300 were carefully mixed. The formulated PEDOT:PSS dispersion was filtered through a 0.45 μm RC filter and spin-coated at 1000 rpm for one minute. The PEDOT:PSS layer was then patterned and annealed for 10 min at 110 °C, cooled, rinsed with isopropanol by spinning at 4000 rpm to remove the excess surfactant (Zonyl) from the surface, and then annealed for another 10 min at the same temperature. The typical thickness of PEDOT:PSS was found to be ~130 nm. The precursor solution was spin-coated (1500 rpm for 20 s and then at 2000 rpm for 5 s) on top. After spin-coating, the substrates were immediately transferred to a hot plate at 110 °C where the colorless wet film is turned into glassy dark brown layer in few seconds and then further annealed for 45 min in ambient air. The procedure resulted in a 350–400 nm thick perovskite absorber layer. PCBM (20 mg/ml in 1:1 volume ratio of chlorobenzene and chloroform) was spin coated (1500 rpm for 15 s and then at 2000 rpm for 15 s) on top of the perovskite layer, which yields a thickness of 50–70 nm. The entire processing up to this step is performed in ambient air. The sample was then transferred to a vacuum chamber located inside a nitrogen-filled glove box for the evaporation of the aluminum top electrode at $<3\times10^{-6}$ mbar. The solar cells were encapsulated with a glass cover using a UV-curable epoxy sealant (Ossila E131), with a UV exposure time of 6 min. The fabricated solar cells with an active area of ~0.17 cm^2 were tested on a LOT-QD solar simulator (LS0821). The radiation intensity was adjusted using a calibrated reference silicon diode to 100 mW/cm^2. External quantum efficiencies (EQEs) were recorded by using a lock-in amplifier (SR830, Stanford Research Systems) and a Jaissle 1002 potentiostat. The potentiostat operated in the two electrode configuration is a high performance current amplifier with a variable gain ranging from 10 to 10^8 V/A. In addition, the potentiostat allows measuring the EQE-spectra at different applied voltages. The devices were illuminated by monochromatic light from a xenon lamp passing through a monochromator (Oriel Cornerstone) with typical intensities in the range of 10–100 μW. A filter wheel holding long-pass filters and a mechanical chopper was mounted between the xenon lamp and the monochromator. Chopping frequencies in the

range of 73–273 Hz were used. A calibrated silicon diode (Hamamatsu S2281) was used as a reference. A halogen lamp (Philips 50 W, 12 V) provided a variable white light bias to the solar cells while the EQE was measured. To determine the power conversion efficiency of the prepared solar cells, the illuminated area of the solar cell was defined using a shadow mask (0.13 cm^2). In a first step the current-voltage curve was recorded with a Keithley 2400 source-measurement unit under illumination (solar simulator). The voltage was increased slowly (20 mV/s) and the current-voltage curve was determined close to steady state-conditions. To check for hysteresis a reverse voltage scan was performed decreasing the voltage by 20 mV/s. In a second step the short circuit current was recorded (steady state value) with a Keithley 2400. A maximum-power-point tracking algorithm was used to measure the steady-state power output of the solar cell. The external quantum efficiency was determined operating the solar cell under short circuit conditions and 1 sun illumination. The short circuit current calculated using the EQE-data allowed the determination of the spectral mismatch factor (MM) of our solar simulator. We found values >0.95 for the investigated devices. This mismatch factor was used to correct the maximum power point measurement. UV–vis absorption spectra of perovskite films were recorded using a double beam UV–vis spectrometer (Perkin Elmer 1050) equipped with an integrating sphere. A Bruker Dektak XT profilometer was used to measure layer thicknesses. Photoluminescence and electroluminescence spectra of various devices were measured using a Shamrock SR-303i monochromator and an Andor iDus Si-CCD. Samples were excited at 473 nm (5 mW) using a solid-state laser or a supercontinuum light source (NKT EXB6) connected to a VIS-NIR SuperK Select Box. A set of long-pass filters was used to avoid any distortion of the recorded spectra by the laser light. Electroluminescence spectra were recorded while applying different potentials with a Keithley 2401. The integrated electroluminescence was detected measuring the emitted photon current with a calibrated large-area Si-photodetector (Hamamatsu S2281) positioned close to the sample. Preliminary stability studies were performed on an ORIEL solar simulator. Surface and cross section scanning electron microscopy (SEM) images were made using a ZEISS 1540XB CrossBeam Scanning microscope equipped with a focused ion-beam (FIB) unit. Gas chromatography coupled with mass spectrometry (GC–MS) measurements were performed on an 6890 GC with a 5935C mass selective detector (both Agilent Technologies, Waldbronn, Germany) equipped with a MPS2-XL headspace autosampler from Gerstel (Mülheim/Ruhr, Germany). The carrier gas used was helium and a ZB-624 GC-column, 60 m $\times$ 0.25 mm I.D. film thickness 1.40 μm (Phenomenex, Aschaffenburg, Germany) was employed. 500 μl of the gas-phase above PEDOT:PSS-films coated on glass substrates was analyzed after the films were heated to 140 °C for 10 min; the MS was operated in the full-scan mode.

3. Results and discussion

3.1. Thin perovskite film

High-quality perovskite films with no voids inside the active layer are a key requirement in making planar perovskite solar cells. We optimized our system by testing different deposition procedures and characterized the resulting films using a scanning electron microscope. Fig. 1 shows different perovskite films deposited on a) glass coated with ITO, b) glass coated with ITO and PEDOT:PSS (Clevios PH1000), c) glass coated with ITO and PEDOT:PSS (Clevios PH1000) processed with 5% v/v DMSO, d) glass coated with ITO and PEDOT:PSS (Clevios PH1000) processed with 0.7% v/v Zonyl® FS-300, glass coated with ITO and PEDOT:PSS (Clevios PH1000) processed with 0.7% v/v Zonyl® FS-300% and 2.5% v/v DMSO e), 5% v/v DMSO f), 10% v/v DMSO g), 15% v/v DMSO h), 20% v/v DMSO i).

The perovskite film on ITO coated glass comprises domains separated by large holes (Fig. 1(a)). Perovskite layers processed on neat PEDOT:PSS show many small holes (Fig. 1(b)). The addition DMSO or Zonyl to PEDOT:PSS reduces the number and size of defects in the perovskite films (Fig. 1(c) and (d)). By using both additives and adding $\geq 5\%$ DMSO continuous layers are formed. The role of the additives DMSO and Zonyl is still not fully understood. DMSO is known to increase the conductivity of PEDOT:PSS films [38]. Zonyl is often used to improve the wettability of the PEDOT:PSS dispersion on hydrophobic substrates [39]. Also the mechanical properties and the surface nano-morphology of PEDOT:PSS layers can be altered by DMSO and Zonyl additives [40]. Alternatively, additives remaining in the deposited film may improve the crystallization of the perovskite on the PEDOT:PSS surface. DMSO is a good solvent for PbI_2, the remaining DMSO may hinder crystallization of PbI_2 at the surface, providing an amorphous seed layer from which a more compact perovskite film can grow [41]. However, preliminary GC–MS investigations on PEDOT:PSS layers deposited with different additive concentrations revealed that the treatments performed after spin-coating removes a significant fraction of the DMSO trapped in the film (Fig. S1). While untreated PEDOT:PSS layers show strong DMSO signals (even for the Clevios PH1000 used as received), all treated samples show a weak DMSO signal with similar amplitudes. This suggests that the surface energy and the nano-morphology of the PEDOT:PSS layer play a crucial role in the formation of the perovskite layer in our process. In our work we found that the formulation PEDOT:PSS (Clevios PH1000) with 0.7% v/v Zonyl® FS-300% and 5% v/v DMSO allows the preparation of efficient solar cells with a high yield and we focused on further investigations on samples processed with this formulation. The basic optical and structural (X-ray) characterizations are summarized in the Supporting Information (Figs. S2 and S3). They show that our process yields typical perovskite material and the films do not contain larger volumes of unreacted lead-halides.

3.2. Solar cell characterization

After optimizing the compact pinhole free perovskite film, solar cells were fabricated with a device architecture of ITO/PEDOT:PSS/Perovskite/PCBM/Al. A schematic of the device layer structure is shown in Fig. 2(a) and a cross-sectional SEM of a solar cell is shown in Fig. 2(b). This cross-section is consistent with the SEM image surface morphology in Fig. 1, where the boundaries between continuous perovskite crystallites are well-resolved, and it is clearly visible that the film is closed. The layer of PCBM can be seen to conformally coat the top of the perovskite film, filling in the space between the tops of adjacent crystallites.

The photovoltaic performances of the solar cells were investigated using three independent methods to ensure consistency and accuracy. Power conversion efficiencies were determined by current-voltage characterization by sweeping the voltage from negative to positive and positive to negative values. The J_{SC} of the devices was calibrated against the integrated external quantum efficiency. Finally, the cells were tested under maximum power point tracking to rule out any hysteresis effects and to observe performance stability. Fig. 3(a) shows current-voltage curve of one of the investigated perovskite solar cells. Only a small hysteresis is visible which is typical for the devices prepared following the procedure described above. Fig. 3(b) shows the corresponding maximum power point scan. The inset is the photo of the encapsulated and contacted solar cell where no changes in color or performance of the solar cells were observed after encapsulation.

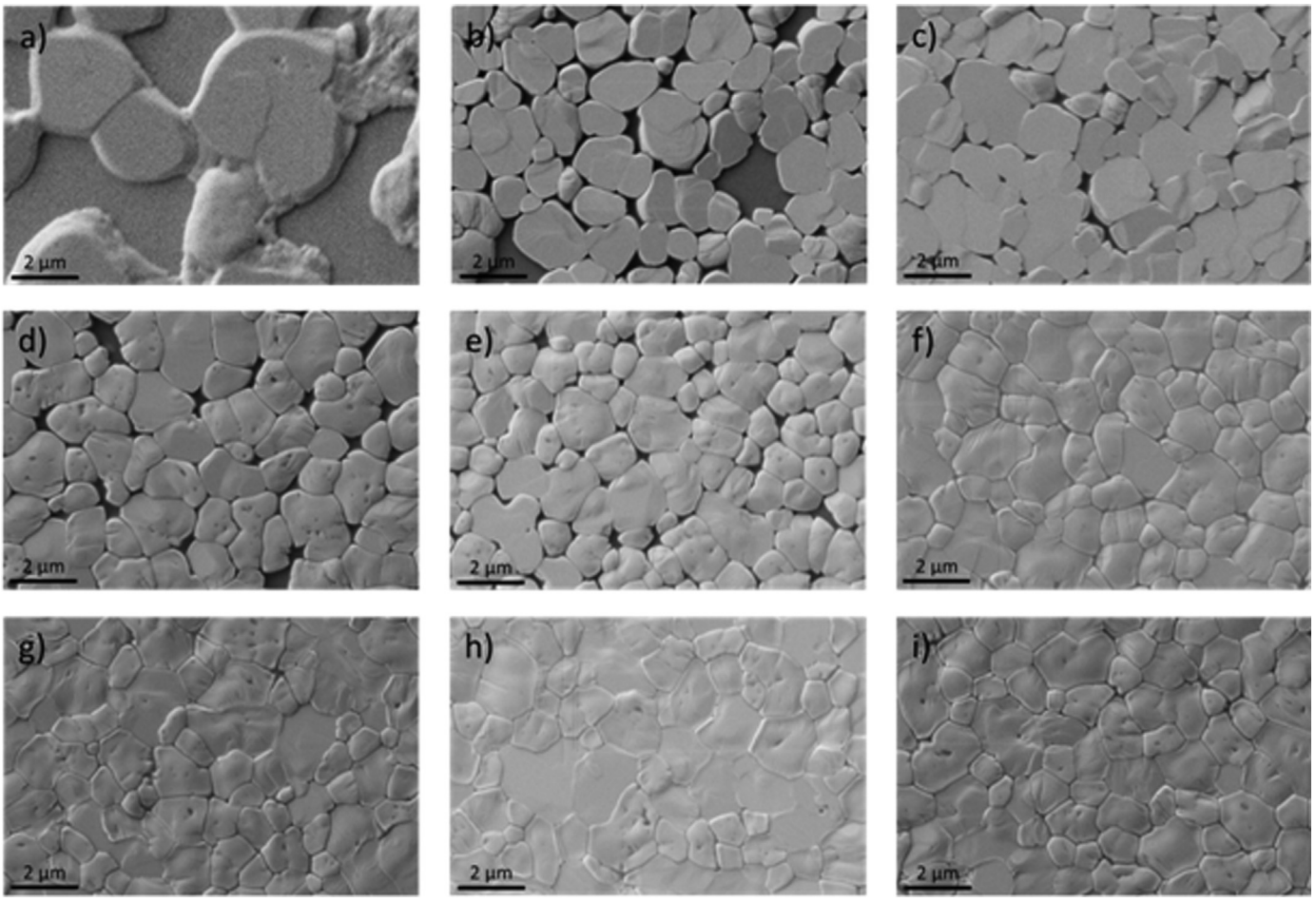

Fig. 1. SEM images of perovskite films coated on top of (a) Glass/ITO, (b) PEDOT:PSS (Clevios PH1000), (c) PEDOT:PSS (Clevios PH1000) processed with 5% v/v DMSO, (d) PEDOT:PSS (Clevios PH1000) processed with 0.7% v/v Zonyl® FS-300, (e) PEDOT:PSS (Clevios PH1000) processed with 0.7% v/v Zonyl® FS-300% and 2.5% v/v DMSO, (f) and 5% v/v DMSO, (g) and 10% v/v DMSO, (h) and 15% v/v DMSO, and (i) and 20% v/v DMSO.

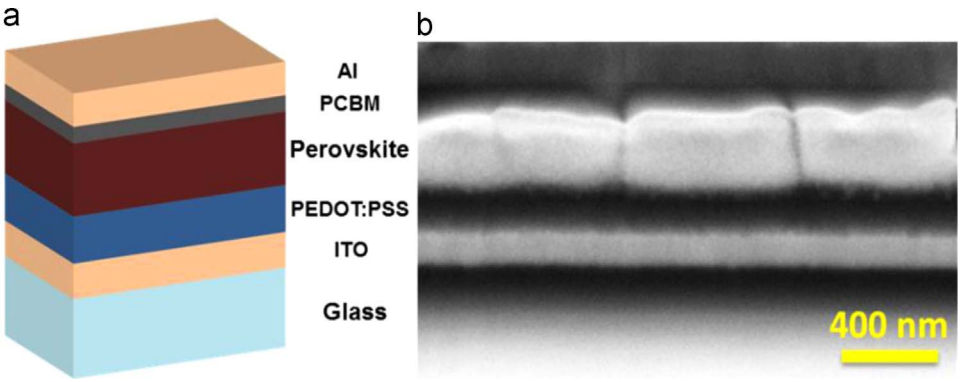

Fig. 2. (a) Schematic diagram of the solar cell stacked layers, and (b) Cross-sectional SEM showing the structure ITO/PEDOT:PSS/Perovskite/PCBM/Al.

Devices do show low leakage currents at reverse bias (Fig. S4a) and good stability when operated under continuous solar illumination (Fig. 3(b)). Under 1 sun illumination, typical devices deliver open circuit voltages in the range of 0.93–0.97 V, fill factors between 0.7 and 0.75, and short circuit currents around 17 mA/cm^2 resulting in power conversion efficiencies in the range of 12–12.5% (Fig. S4b). Current-voltage curves shown in Fig. 3(a) are corrected for the spectral mismatch of the solar simulator by external quantum efficiency measurements. The corresponding EQE-spectrum is shown in Fig. 4(a).

The EQE peaks around 550 nm, reaching a maximum external quantum efficiency of ~80%. In the blue (300–450 nm) and the near-IR (650–800 nm) the spectral response is substantially smaller leading to a significant reduction of the photocurrent. This loss can be attributed to parasitic absorption in the ITO (300–450 nm) and the PEDOT:PSS layer (both spectral regions) as well as the poor reflectance of the metal back electrode (aluminum). Due to the roughness of the perovskite/PCBM bilayer, the 110 nm thick aluminum layer deposited as top electrode is a poor reflector. Studying the light bias and the reverse bias dependence of the EQE spectrum shows that neither a dc-illumination up to 1 sun nor negative voltages up to −1 V changes the EQE spectrum (Fig. S5). This illustrates that under short circuit conditions charge carrier extraction is essentially complete. In addition the absence of a

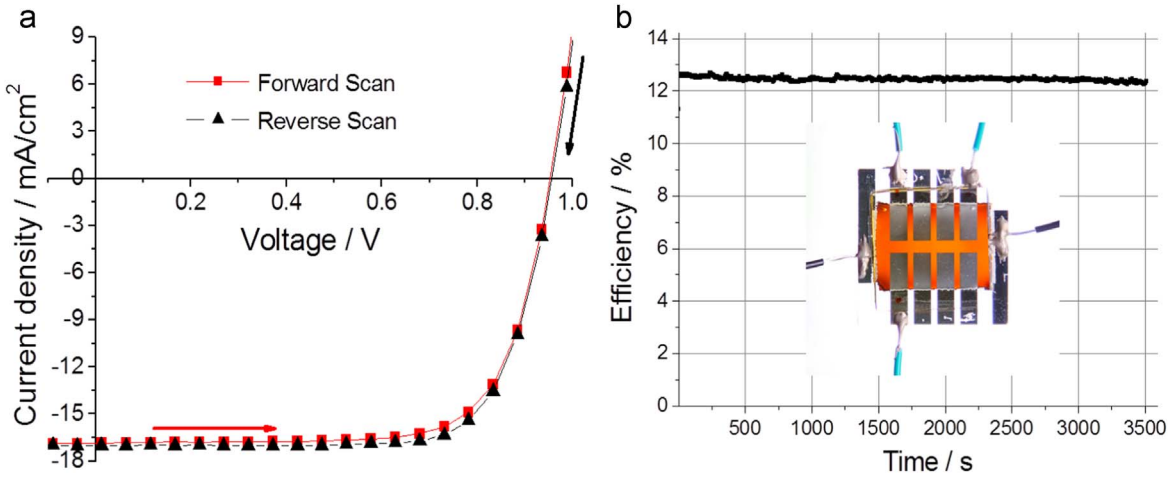

Fig. 3. (a) Current-voltage curve of the perovskite solar cell, forward and reverse scan 20 mV/s. (b) Maximum power point scan corrected for the spectral mismatch. The inset is the photo of the encapsulated and contacted solar cell.

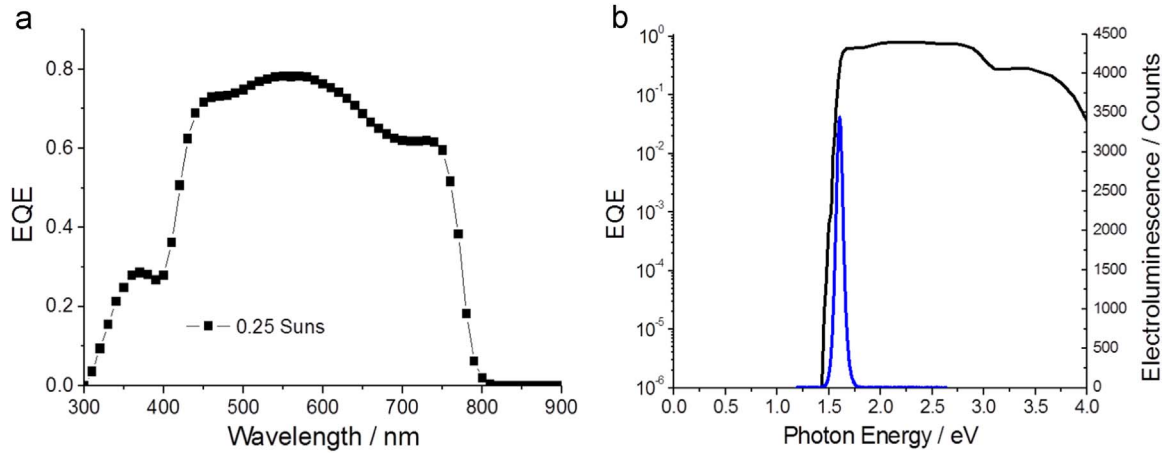

Fig. 4. (a) External quantum efficiency spectrum measured under 0.25 suns white-light bias, and (b) EQE spectrum and electroluminescence spectrum of the same perovskite solar cell.

light bias dependence confirms that the short circuit current scales linearly with the light intensity [42]. Fig. 4(b) shows the EQE spectrum of a typical device on a logarithmic scale. The EQE decreases rapidly below 1.5 eV suggesting that the number of photoactive states in the absorber band gap is very small. The electroluminescence of the same device is also shown in Fig. 4(b) with a narrow emission peaking at ~1.6 eV or 775 nm. Applying the relations first derived by Rau [43] and later on used by various different authors [33,44], the radiative limit of the open circuit voltage ($V_{oc,rad}$) and the power conversion efficiency of a solar cell can be determined. The current-voltage curve of an ideal photovoltaic device, with only radiative recombination of charge carriers allowed, is given by

$$J = J_{0,rad} \times \left[\exp\left(\frac{qV}{k_B T} \right) - 1 \right] - J_{pH} \quad (1)$$

where J is the current density, $J_{0,rad}$ is the diode saturation current, q is the unit charge, V is the applied bias, k_B is the Boltzmann constant, T the temperature and J_{PH} is the photocurrent density. According to Rau, $J_{0,rad}$ can be calculated by

$$J_{0,rad} = q \times \int EQE_{PV}(E) \times \Phi_{BB}(E)\, dE \quad (2)$$

where EQE_{PV} is the external quantum efficiency of the solar cell and Φ_{BB} is the spectral photon flux at 300 K. J_{PH} can be calculated in the same way by replacing the 300 K black body radiation by the Air Mass 1.5 Gobal (AM1.5 G) spectrum. The rearrangement of Eq. (1) leads to

$$V_{oc,rad} = \frac{k_B T}{q} \times \ln\left(\frac{J_{PH}}{J_{0,\ rad}} + 1 \right) \quad (3)$$

This analysis does not include Ohmic or any non-radiative recombination losses. Therefore it gives an upper performance limit for the device with known external quantum efficiency. Calculated parameters for four typical devices prepared within this study are summarized in Table 1. The large difference between the measured and the calculated radiative open circuit voltage suggests that non-radiative recombination plays an important role in the studied devices. By measuring the photon flux of electroluminescence emitted by the solar cell ($J_{em}(V)$) when operated under forward bias at different injection currents $J_{inj}(V)$, the external quantum efficiency of the LED ($EQE_{LED}(V)$) can be determined. $EQE_{LED}(V)$ is given by $J_{em}(V)/J_{inj}(V)$ and the value is closely related to the external-radiative efficiency (ERE) defined by Green [45]. If the $EQE_{LED} < 1$, $J_{0,rad}$ in Eqs. 1 and 3 need to be replaced by $J_{0,rad}/EQE_{LED}$, where the EQE_{LED} is determined at current densities comparable to the photocurrent density generated by AM1.5 G solar radiation.

For all investigated solar cells we find $EQE_{LED} < 10^{-6}$ (Fig. 5 and Fig. S6). Recalculating the open circuit voltages using Eq. (3) and including EQE_{LED}, values close to the actual measured voltages are found. All data are summarized in Table 2.

Table 1
Calculated parameters for devices prepared within this study using Eqs. (1)–(3) and the corresponding EQE spectra.

	$J_{0,rad}$ [mA/cm^2]	J_{PH} [mA/cm^2]	$V_{oc,rad}$ [V]	$V_{oc,measured}$ [V]	ΔV_{oc} [V]
Device 1	1.14×10^{-21}	16.70	1.32	0.97	0.35
Device 2	1.14×10^{-21}	16.66	1.32	0.96	0.36
Device 3	1.24×10^{-21}	16.83	1.32	0.94	0.38
Device 4	1.55×10^{-21}	17.10	1.31	0.97	0.34

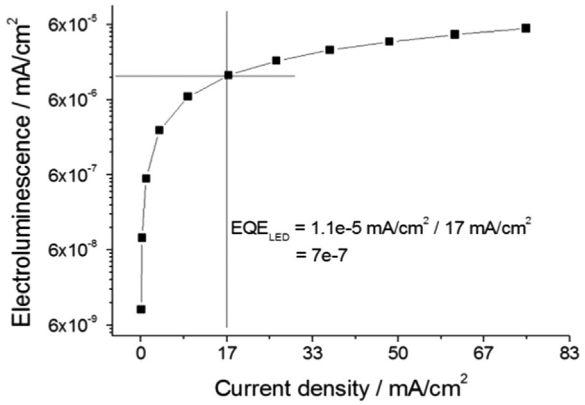

Fig. 5. Electroluminescence versus driving current measured on one of the prepared solar cells.

Table 2
Calculated EQE_{LED}, V_{OC} corrected and V_{OC} measured for four typical devices using Eq. (3).

	EQE_{LED}	$V_{oc,cor}$ [mV]	$V_{oc,measured}$ [mV]
Device 1	7×10^{-7}	0.954	0.97
Device 2	7×10^{-7}	0.954	0.96
Device 3	4×10^{-7}	0.937	0.94
Device 4	8×10^{-7}	0.95	0.97

Eq. (1) can also be used to determine the maximum power conversion efficiency of the studied devices assuming only radiative recombination and no electrical losses due to serial or parallel parasitic resistors. With the measured EQE_{PV} and, considering only radiative recombination leads to a maximum efficiency of 20% (V_{OC} = 1.32 V, FF = 91%, I_{SC} = 16.7 mA/cm^2), Eq. (1) predicts a power conversion efficiency of 14% (V_{OC} = 0.95 V, FF = 88%, I_{SC} = 16.7 mA/cm^2) when the measured EQE_{LED} is included. Photoluminescence spectra of a solar cell recorded at −1 V, under short circuit and open circuit conditions, are shown in Fig. 6(a). The sample is excited using a diode-laser (473 nm) and the solar cell delivers a current of 0.6 mA (equivalent to ~0.2 suns). The spectrum comprises an emission which does not depend on the applied bias and a feature around 1.6 eV which increases with increasing bias. Fig. 6(b) shows photoluminescence (PL) spectra recorded at various different biases corrected with the spectrum recorded at −1 V. As discussed by Tvingstedt et al. this bias-dependent photoluminescence is a signature of an ideal solar cell [46]. While at short circuit the photoluminescence should be quenched, at open circuit photo-induced charges recombine radiatively. In the studied devices a residual PL-signal is found at I_{sc} which increases exponentially upon increasing the bias voltage (Fig. 6(c)). The principle of detailed balance dictates the emitted photon flux (Φ_{em}) is proportional to $EQE_{PV}(E)$ times the black body radiation at 300 K (Φ_{BB}). Therefore, the spectrum calculated via $EQE_{PV}(E) \times \Phi_{BB}(E)$ should reproduce the photoluminescence and electroluminescence of the corresponding solar cell. In Fig. 6 (d) a comparison of the three spectra is shown indicating close overlap. At lower energy, *i.e.* in the spectral region where the EQE is very small, the calculated spectrum shows some deviations from the PL and EL spectrum (Fig. S7). The detailed analysis above reveals that the devices studied here show the typical characteristics of planar perovskite solar cells. However, compared to mesoscopic and planar devices using TiO_2 or Al_2O_3 as interfacial layers on the transparent conductive oxide or some devices deposited via vapor deposition, the investigated devices show a smaller open circuit voltage. The presented results suggest that the low quantum yield of radiative recombination causes the observed open circuit voltage loss.

Tvingstedt et al. reported an EQE_{LED} of 1.2×10^{-4} and an open circuit voltage of 1.08 V for an inverted, vapor-processed $CH_3NH_3PbI_3$-PCBM solar cell [42]. A one-hundred times smaller EQE_{LED} leads to a V_{oc} loss of ~50 mV, resulting in an open circuit voltages observed for our devices. Therefore one obvious strategy to improve the performance of the studied solar cells is reducing the non-radiative recombination of photo-induced charges. Defects in the absorber layer, and at interfaces/surfaces may act as recombination centers. Further optimization of the growth conditions may reduce the number of defects in the perovskite film. The choice of alternative interlayers may also help improving the radiative recombination quantum yield in our solar cells. As shown in Fig. S2, using PEDOT:PSS and PCBM leads to a strong quenching of the perovskite photoluminescence, suggesting that these widely-used interlayers are not ideal candidates. Alternative interlayers leading to less PL-quenching while still supporting selective charge extraction should also lead to higher open circuit voltages.

Preliminary device simulation work suggests that bulk-recombination plays an important role in the investigated devices. Current-voltage curves recorded in the dark and under illumination can be simulated reasonably well by using a simple replacement circuit based on the diodes with an ideality-factor n of 1 and 2 connected in parallel. A 1-diode model requires an ideality factor around 1.75 and a diode saturation current (~1×10^{-7} mA/cm^2). In classical inorganic solar cells an ideality factor 1 is related to band-to-band recombination while n = 2 is often interpreted as recombination that occurs via deep-level states or at interfaces and grain boundaries [47,48]. Eq. (1) also predicts that devices should show a FF > 85% at solar illumination intensities while prepared devices show fill factors ≤ 75%. We attribute the lower fill factor to Ohmic losses. Investigated devices showed a serial resistance around 25 Ω and a parallel resistance around 6 kΩ. As shown in Fig. S8, the fill factor of our devices increases upon decreasing the illumination intensity. This suggests that the serial resistance is too high and additional bus bars and electrodes with a lower sheet resistance could increase the overall efficiency of the prepared devices. Also the losses in the EQE_{PV} could be reduced by improving the optical design of the solar cell. An anti-reflection coating on the front side of the device, transparent electrode and interfacial layers with smaller absorbance and a high quality reflector as back electrode could lead to higher external quantum efficiencies (EQE_{PV} and EQE_{PL}) and to larger short circuit current and open circuit voltage.

In summary, we have developed a simple and reliable manufacturing process for planar perovskite solar cells comprising

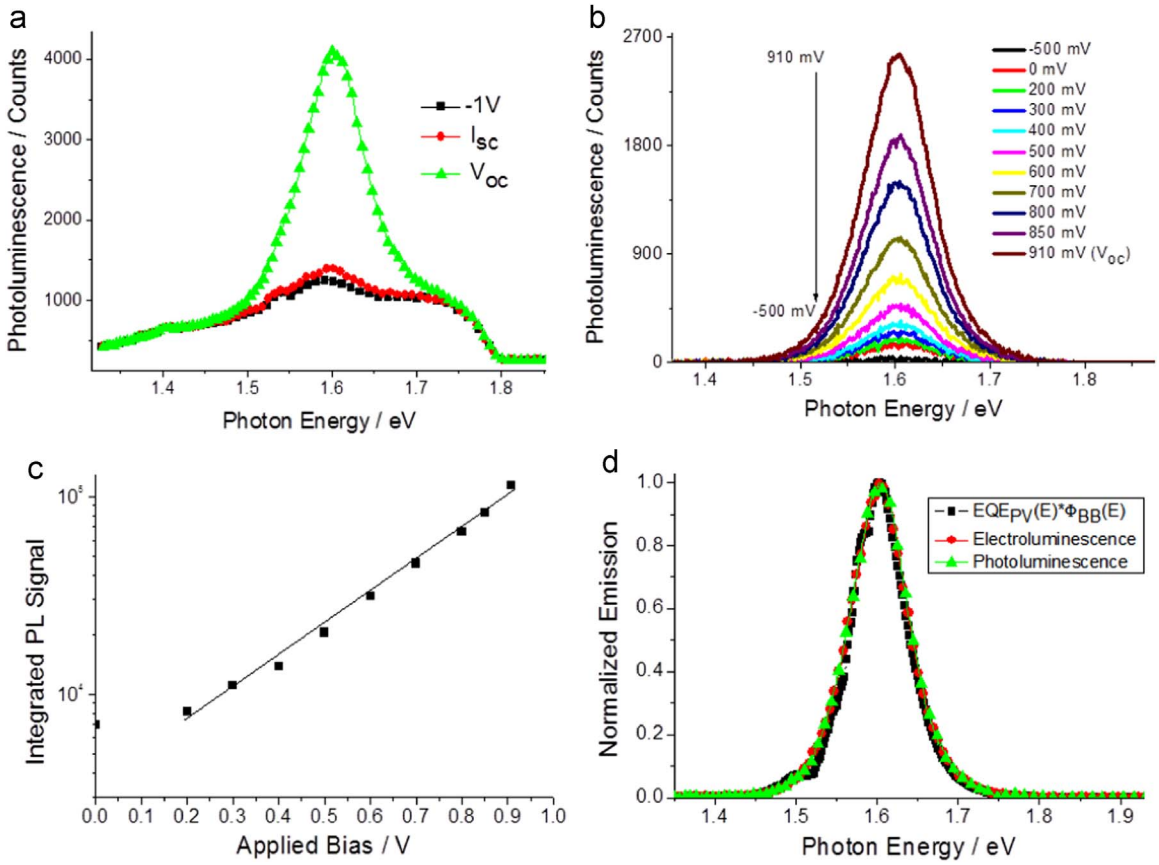

Fig. 6. Photoluminescence (a) measured at −1 V, short circuit and open circuit condition, (b) measured at various voltage biases, (c) Signal intensity as a function of applied voltage bias. (d) Electroluminescence, $EQE_{PV}(E) \times \Phi_{BB}(E)$ spectra.

PEDOT:PSS and PCBM as interfacial layers. We found that the use of DMSO and Zonyl as processing additives for the used PEDOT:PSS affects the quality of the perovskite absorber layer processed on top of this layer. Prepared devices show a good operational stability and a moderate hysteresis when the current-voltage curve is recorded at 20 mV/s in forward and reverse direction. The radiative recombination quantum yield is found to be small, leading to observed losses in the open circuit voltage. Our analysis shows that this type of perovskite solar cells can reach efficiencies of 20% upon reducing optical, electrical, and non-radiative recombination losses. Replacing the PEDOT:PSS hole transport layer with a material that does not quench the photo- and electroluminescence is the key step to realizing the full potential.

Acknowledgment

We would like to acknowledge the Austrian Research Promotion Agency (FFG) (flex! PV KOOP-IF 838621) and the Austrian Science Fund FWF (Wittgenstein Prize of N.S. Sariciftci Z222-N19) for financial support. Sekai Tombe gratefully acknowledges the financial support from L'Oréal-UNESCO For Women In Science Sub-Saharan Africa and the National Research Foundation of South Africa (NRF).

Appendix A. Supporting information

Supplementary data associated with this article can be found in the online version at http://dx.doi.org/10.1016/j.solmat.2016.05.011.

References

[1] J.H. Noh, S.H. Im, J.H. Heo, T.N. Mandal, S.I. Seok, Chemical management for colorful, efficient, and stable inorganic–organic hybrid nanostructured solar cells, Nano Lett. 13 (2013) 1764–1769.
[2] S.D. Stranks, G.E. Eperon, G. Grancini, C. Menelaou, M.J.P. Alcocer, T. Leijtens, L. M. Herz, A. Petrozza, H.J. Snaith, Electron-hole diffusion lengths exceeding 1 μm in an organometal trihalide perovskite absorber, Science 342 (2013) 341–344.
[3] G. Xing, N. Mathews, S. Sun, S.S. Lim, Y.M. Lam, M. Grätzel, S. Mhaisalkar, T. C. Sum, Long-range balanced electron- and hole-transport lengths in organic-inorganic $CH_3NH_3PbI_3$, Science 342 (2013) 344–347.
[4] C.S. Ponseca, J.T.J. Savenije, M. Abdellah, K. Zheng, A. Yartsev, T. Pascher, T. Harlang, P. Chabera, T. Pullerits, A. Stepanov, J.P. Wolf, V. Sundström, Organometal halide perovskite solar cell materials rationalized: ultrafast charge generation, high and microsecond-long balanced mobilities, and slow recombination, J. Am. Chem. Soc. 136 (2014) 5189–5192.
[5] H. Zhou, Q. Chen, G. Li, S. Luo, T.B. Song, H.S. Duan, Z. Hong, J. You, Y. Liu, Y. Yang, Interface engineering of highly efficient perovskite solar cells, Science 345 (2014) 542–546.
[6] N.J. Jeon, J.H. Noh1, W.S. Yang, Y.C. Kim, S. Ryu, J. Seo, S.I. Seok, Compositional engineering of perovskite materials for high-performance solar cells, Nature 517 (2015) 476–480.
[7] W.S. Yang, J.H. Noh, N.J. Jeon, Y.C. Kim, S. Ryu, J. Seo, S. Il Seok, High-performance photovoltaic perovskite layers fabricated through intramolecular exchange, Science 348 (2015) 1234–1237.
[8] J.H. Im, I.H. Jang, N. Pellet, M. Grätzel, N.G. Park, Growth of $CH_3NH_3PbI_3$ cuboids with controlled size for high-efficiency perovskite solar cells, Nat. Nanotechnol. 9 (2014) 927–932.
[9] M. Liu, M.B. Johnston, H.J. Snaith, Efficient planar heterojunction perovskite solar cells by vapour deposition, Nature 501 (2014) 395–398.
[10] J. Burschka, N. Pellet, S.J. Moon, R.H. Baker, P. Gao, M.K. Nazeeruddin, M. Grätzel, Sequential deposition as a route to high-performance perovskite-sensitized solar cells, Nature 499 (2013) 316–319.
[11] A. Mei, X. Li, L. Liu, Z. Ku, T. Liu, Y. Rong, M. Xu, M. Hu, J. Chen, Y. Yang, M. Grätzel, H. Han, A hole-conductor-free, fully printable mesoscopic perovskite solar cell with high stability, Science 345 (2014) 295–298.
[12] A. Kojima, K. Teshima, Y. Shirai, T. Miyasaka, Organometal halide perovskites as visible-light sensitizers for photovoltaic cells, J. Am. Chem. Soc. 131 (2009) 6050–6051.

[13] W.-J. Yin, J.-H. Yang, J. Kang, Y. Yan, S.-H. Wei, Halide perovskite materials for solar cells: a theoretical review, J. Mater. Chem. A 3 (2015) 8926–8942.
[14] W.-J. Yin, T. Shi, Y. Yan, Unique properties of halide perovskites as possible origins of the superior solar cell performance, Adv. Mater. 26 (2014) 4653–4658.
[15] H.J. Snaith, A. Abate, J.M. Ball, G.E. Eperon, T. Leijtens, N.K. Noel, S.D. Stranks, J. T.W. Wang, K. Wojciechowski, W. Zhang, Anomalous hysteresis in perovskite solar cells, J. Phys. Chem. Lett. 5 (2014) 1511–1515.
[16] E.L. Unger, E.T. Hoke, C.D. Bailie, W.H. Nguyen, A.R. Bowring, T. Heumüller, M. G. Christoforo, M.D. McGehee, Hysteresis and transient behavior in current–voltage measurements of hybrid-perovskite absorber solar cells, Energy Environ. Sci. 7 (2014) 3690–3698.
[17] J.M. Frost, K.T. Butler, A. Walsh, Molecular ferroelectric contributions to anomalous hysteresis in hybrid perovskite solar cells, APL Mater. 2 (2014) 081506.
[18] R.S. Sanchez, V.G. Pedro, J.W. Lee, N.G. Park, Y.S. Kang, I.M. Sero, J. Bisquert, Slow dynamic processes in lead halide perovskite solar cells. Characteristic times and hysteresis, J. Phys. Chem. Lett. 5 (2014) 2357–2363.
[19] M. Grätzel, The light and shade of perovskite solar cells, Nat. Mater. 13 (2014) 838–842.
[20] M.M. Lee, J. Teuscher, T. Miyasaka, T.N. Murakami, H.J. Snaith, Efficient hybrid solar cells based on meso-superstructured organometal halide perovskites, Science 338 (2012) 643–647.
[21] K. Wojciechowski, M. Saliba, T. Leijtens, A. Abate, H.J. Snaith, Sub-150 °C processed meso-superstructured perovskite solar cells with enhanced efficiency, Energy Environ. Sci. 7 (2014) 1142–1147.
[22] D. Liu, T.L. Kelly, Perovskite solar cells with a planar heterojunction structure prepared using room-temperature solution processing techniques, Nat. Photonics 8 (2014) 133–138.
[23] J. You, Z. Hong, Y.M. Yang, Q. Chen, M. Cai, T.B. Song, C.C. Chen, S. Lu, Y. Liu, H. Zhou, Y. Yang, Low-temperature solution-processed perovskite solar cells with high efficiency and flexibility, ACS Nano 8 (2014) 1674–1680.
[24] J.S.S. Park, Y.C. Kim, N.J. Jeon, J.H. Noh, S.C. Yoon, S.I. Seok, Benefits of very thin PCBM and LiF layers for solution-processed p–i–n perovskite solar cells, Energy Environ. Sci. 7 (2014) 2642–2646.
[25] P. Docampo, J.M. Ball, M. Darwich, G.E. Eperon, H.J. Snaith, Efficient organometal trihalide perovskite planar-heterojunction solar cells on flexible polymer substrates, Nat. Commun. 4 (2013) 2761.
[26] W. Nie, H. Tsai, R. Asadpour, J.-C. Blancon, A.J. Neukirch, G. Gupta, J.J. Crochet, M. Chhowalla, S. Tretiak, M.A. Alam, H.-L. Wang, A.D. Mohite, High-efficiency solution-processed perovskite solar cells with millimeter-scale grains, Science 347 (2015) 522–525.
[27] M. Kaltenbrunner, M.S. White, E.D. Głowacki, T. Sekitani, T. Someya, N. S. Sariciftci, S. Bauer, Ultrathin and lightweight organic solar cells with high flexibility, Nat. Commun. 3 (2012) 770.
[28] M. Kaltenbrunner, G. Adam, E.D. Głowacki, M. Drack, R. Schwödiauer, L. Leonat, D.H. Apaydin, H. Groiss, M.C. Scharber, M.S. White, N.S. Sariciftci, S. Bauer, Flexible high power-per-weight perovskite solar cells with chromium oxide–metal contacts for improved stability in air, Nat. Mater. 14 (2015) 1032–1039.
[29] Q. Chen, H. Zhou, Z. Hong, S. Luo, H.S. Duan, H.H. Wang, Y. Liu, G. Li, Y. Yang, Planar heterojunction perovskite solar cells via vapor-assisted solution process, J. Am. Chem. Soc. 136 (2014) 622–625.
[30] N.J. Jeon, J.H. Noh, Y.C. Kim, W.S. Yang, S. Ryu, S.I. Seok, Solvent engineering for high-performance inorganic–organic hybrid perovskite solar cells, Nat. Mater. 13 (2014) 897–903.
[31] S. Sun, T. Salim, N. Mathews, M. Duchamp, C. Boothroyd, G. Xing, T.C. Sumbce, Y.M. Lam, The origin of high efficiency in low-temperature solution-processable bilayer organometal halide hybrid solar cells, Energy Environ. Sci. 7 (2014) 399–407.
[32] Y. Zhao, K. Zhu, CH_3NH_3Cl-assisted one-step solution growth of $CH_3NH_3PbI_3$: structure, charge-carrier dynamics, and photovoltaic properties of perovskite solar cells, J. Phys. Chem. C 118 (2014) 9412–9418.
[33] B. Suarez, V.G. Pedro, T.S. Ripolles, R.S. Sanchez, L. Otero, I.M. Sero, Recombination study of combined halides (Cl, Br, I) perovskite solar cells, J. Phys. Chem. Lett. 5 (2014) 1628–1635.
[34] X. Huang, K. Wang, C. Yi, T. Meng, X. Gong, Efficient perovskite hybrid solar cells by highly electrical conductive PEDOT:PSS hole transport layer, Adv. Energy Mater. 6 (2016) 1501773.
[35] Z. Yong, H. Xiaotian, C. Lie, H. Zengqi, F. Qingxia, L. Yawen, Z. Lin, C. Yiwang, Flexible, hole transporting layer-free and stable $CH_3NH_3PbI_3$/PC 61BM planar heterojunction perovskite solar cells, Org. Electron 30 (2016) 281–288.
[36] Z. Yang, C.-C. Chueh, F. Zuo, J.H. Kim, P.-W. Liang, K.-Y.A. Jen, High-performance fully printable perovskite solar cells via blade-coating technique under the ambient condition, Adv. Energy Mater. 5 (2015) 1500328.
[37] W. Tress, N. Marinova, O. Inganäs, M.K. Nazeeruddin, S.M. Zakeeruddin, M. Grätzel, Predicting the open-circuit voltage of $CH_3NH_3PbI_3$ perovskite solar cells using electroluminescence and photovoltaic quantum efficiency spectra: the role of radiative and non-radiative recombination, Adv. Energy Mater. 5 (2015) 1400812.
[38] R. Po, C. Carbonera, A. Bernardi, F. Tinti, N. Camaioni, Polymer- and carbon-based electrodes for polymer solar cells: Toward low-cost, continuous fabrication over large area, Sol. Energy Mater. Sol. Cells 100 (2012) 97–114.
[39] M.M. Voigt, R.C.I. Mackenzie, C.P. Yau, P. Atienzar, J. Dane, P.E. Keivanidis, D.D. C. Bradley, J. Nelson, Gravure printing for three subsequent solar cell layers of inverted structures on flexible substrates, Sol. Energy Mater. Sol. Cells 95 (2011) 731–734.
[40] S. Savagatrup, E. Chan, S.M. Renteria-Garcia, A.D. Printz, A.V. Zaretski, T. F. O'Connor, D. Rodriquez, E. Valle, D.J. Lipomi, Plasticization of PEDOT:PSS by common additives for mechanically robust organic solar cells and wearable sensors, Adv. Funct. Mater. 25 (2015) 427–436.
[41] Y. Wu, A. Islam, X. Yang, C. Qin, J. Liu, K. Zhang, W.W. Peng, L. Han, Retarding the crystallization of PbI_2 for highly reproducible planar-structured perovskite solar cells via sequential deposition, Energy Environ. Sci. 7 (2014) 2934–2938.
[42] D.J. Wehenkel, K.H. Hendriks, M.M. Wienk, R.A.J. Janssen, The effect of bias light on the spectral responsivity of organic solar cells, Org. Electron. 13 (2012) 3284–3290.
[43] U. Rau, Reciprocity relation between photovoltaic quantum efficiency and electroluminescent emission of solar cells, Phys. Rev. B 76 (2007) 085303.
[44] U. Rau, U.W. Paetzold, T. Kirchartz, Thermodynamics of light management in photovoltaic devices, Phys. Rev. B 90 (2014) 035211.
[45] M.A. Green, Radiative efficiency of state-of-the-art photovoltaic cells, Prog. Photovolt: Res. Appl. 20 (2012) 472–476.
[46] K. Tvingstedt, O. Malinkiewicz, A. Baumann, C. Deibel, H.J. Snaith, V. Dyakonov, H.J. Bolink, Radiative efficiency of lead iodide based perovskite solar cells, Sci. Rep. 4 (2014) 6071.
[47] J.F. Geisz, M.A. Steiner, I. Garcıa, S.R. Kurtz, D.J. Friedman, Enhanced external radiative efficiency for 20.8% efficient single-junction GaInP solar cells, Appl. Phys. Lett. 103 (2013) 041118.
[48] J. You, Y.M. Yang, Z. Hong, T.-B. Song, L. Meng, Y. Liu, C. Jiang, H. Zhou, W.-H. Chang, G. Li, Y. Yang, Moisture assisted perovskite film growth for high performance solar cells, Appl. Phys. Lett. 105 (2014) 183902.